

doi.org/10.1002/elan.202100484

# On the Integration of Dielectrometry into Electrochemical Impedance Spectroscopy to Obtain Characteristic Properties of a Dielectric Thin Film

Benedikt Sapotta,<sup>[a]</sup> Matthias Schwotzer,<sup>[a]</sup> Christof Wöll,<sup>[a]</sup> and Matthias Franzreb<sup>\*,[a]</sup>

**Abstract:** We demonstrate a novel impedimetric approach providing unprecedented insight into characteristic properties of dielectric thin films covering electrode surfaces. The concept is based on the joint interpretation of electrochemical impedance spectroscopy (EIS) together with dielectrometry (DEM) whose informative value is mutually interconnected. The advantage lies in the synergistic compensation of individual shortcomings ad-

versely affecting conventional impedimetric analysis strategies relying exclusively on either DEM or the traditional EIS approach, which in turn allows a reliable determination of thickness and permittivity values. The versatility of the method proposed is showcased by an in-situ growth-monitoring of a nanoporous, crystalline thin film (HKUST-1) on an interdigitated electrode geometry.

**Keywords:** impedance spectroscopy · interdigitated electrodes · dielectric thin film

## 1 Introduction

The impedance response of a dielectric thin film covering an electrode surface is relevant for a multitude of research fields and applications. In corrosion science for example, impedimetric analysis provides a unique opportunity to characterize the formation of the corrosion layers [1–4] or, conversely, to optimize the formulation of polymeric anti-corrosion coatings on metallic (i.e. electrode) surfaces [5,6]. On the other hand, the variation of the relative permittivity of a dielectric film supported on an electrode surface is used for chemocapacitive gas sensing, an application where the affinity of appropriate layers to target molecules is exploited [7–10]. In electrochemical immunosensing, dielectric films are frequently employed in the form of electrode surface functionalizations with receptor molecules [11,12]. The binding of target molecules to the receptor surface is detected with a change in the impedimetric signal of the immunosensor. [SB(1)]

Electrochemical impedance spectroscopy (EIS) and dielectrometry (DEM) are two impedance techniques [13], which have been used to study characteristic properties of a dielectric film covering an electrode surface, such as coating thickness  $d_C$  and the relative permittivity of the coating  $\epsilon_{r,C}$  [1,14]. IUPAC refers to DEM as an impedimetric technique dedicated to the measurement of the relative permittivity (dielectric constant) of a sample [13]. For a DEM analysis of a dielectric thin film, the coated electrodes are immersed in an electrically insulating reference medium of known permittivity  $\epsilon_{r,M}$ . The resulting impedance signal is expected to be purely capacitive and can be transformed into an effective permittivity value  $\epsilon_{r,eff}$  when the electrode geometry is accounted for.  $\epsilon_{r,eff}$  in turn is a function of both  $\epsilon_{r,C}$  and  $\epsilon_{r,M}$  as well as the volumetric relationship between coating and reference

medium with respect to the electric field propagation inside the electrode geometry. In case the resulting capacitance is measured with the coated electrode exposed to at least two different insulating reference media, it is possible to estimate both  $\epsilon_{r,C}$  and  $d_C$  by modelling the effective permittivity for the given electrode geometry as outlined in detail by Zaretsky et al. [14,15]. However, the interpretation of  $\epsilon_{r,eff}$  should be treated with caution as it is subject to a number of simplistic assumptions such as an idealized homogeneous coating whose dielectric properties do not change depending on the medium it is exposed to. For this reason, DEM alone does not provide a broad framework for a detailed analysis of a dielectric coating.

In a frequently encountered EIS setup to analyze dielectric coatings [3], electrodes are immersed in a conductive reference medium, an electrolyte, containing solvated ions as charge carriers. The corresponding impedance spectrum is comprised of a superposition of various electrochemical effects broadly related to the ionic movement towards and interaction with the respec-

[a] B. Sapotta, M. Schwotzer, C. Wöll, M. Franzreb  
Institute of Functional Interfaces (IFG), Karlsruhe Institute of Technology (KIT), 76344 Eggenstein-Leopoldshafen, Germany  
E-mail: matthias.franzreb@kit.edu

Supporting information for this article is available on the WWW under <https://doi.org/10.1002/elan.202100484>

© 2021 The Authors. Electroanalysis published by Wiley-VCH GmbH. This is an open access article under the terms of the Creative Commons Attribution License, which permits use, distribution and reproduction in any medium, provided the original work is properly cited.

tive countercharged electrode surfaces. In this regard, a dielectric layer covering the electrode surface effectively acts as a diffusion barrier causing ions i.e., charge to accumulate at its outer surface imparting the so-called coating capacitance  $C_C$ . The value of  $C_C$  depends on  $d_C$  as well as  $\epsilon_{r,C}$  which, as opposed to DEM, cannot be directly estimated by this EIS approach. For this reason, interpretation of  $C_C$  is often accomplished with the help of an educated guess for either  $d_C$  or  $\epsilon_{r,C}$ . However, in contrast to DEM, EIS may provide additional information on the ionic permeability of the dielectric layer or may detect the presence of pinholes or cracks exposing the bare electrode surface to the electrolyte.

In this study, we demonstrate that substantial added value can be obtained by integrating DEM into EIS for analyzing thin, dielectric films. Since the prerequisites of the two techniques are apparently inconsistent, with DEM calling for an insulating and the conventional EIS approach for a conducting reference medium, we will briefly summarize the theoretical background in the second chapter. As DEM requires the thin film to comprise a sizeable fraction of the total volume exposed to the electric field, we focus primarily on interdigitated electrode (IDE) geometries which are highly sensitive to changes occurring in close proximity to their electrode surface. In addition, IDEs have the advantage of providing an easily replicable, standardized electrode geometry whose impedimetric response has already been extensively studied [15–18]. To showcase the versatility of the method outlined in the second chapter, we will demonstrate its application for an in-situ growth monitoring of a copper-benzenetricarboxylate surface mounted metal organic framework (HKUST-1 SURMOF) thin film. We chose the HKUST-1 SURMOF as a model thin film as it grows in a well understood, highly self-limiting layer-by-layer fashion [19]. HKUST-1 is a nanoporous, crystalline material comprised of dimeric copper metal centers interconnected by 1,3,5 tricarboxylate units. The spatial arrangement within the HKUST-1 crystal lattice leaves room for three types of pores estimated at 0.5, 1.1 and 1.35 nm in diameter [20]. As a result, metal organic frameworks such as HKUST-1 are able to host guest molecules in its internal pores and have been explored for various sensing applications based on quartz crystal microbalance [21,22], capacitive [23], colorimetric [24], and localized surface plasmon techniques [25]. The results of our impedimetric studies are compared to permittivity values found in the literature and are corroborated by cross section micrographs obtained from scanning electron microscopy (SEM).

## 2 Outline of Method

Impedance spectroscopy is based on measuring a system's sinusoidal current response when applying an ac input voltage or vice versa. A spectrum is taken through variation of the ac frequency which provides access to the frequency dependent amplitudes of and phase shifts

between voltage and current signals. Interpretation of impedance data requires an understanding of the relevant phenomena of influence which can be conceptualized in the form of an equivalent circuit model (ECM). An overview of the ECMs considered in this study is given in Figure 1. In the case of impedance data taken under non-faradaic conditions with uncoated electrodes, ECM 1 shown in Figure 1(A) provides a useful starting point for analysis [18]. ECM 1 is based on three equivalent circuit elements separated into two distinctive branches. The upper branch accounts for the displacement and polarization current passing through the electrode setup induced by a change in electric field strength which is bundled into the geometric capacitance parameter  $C_{Geo}$ .  $C_{Geo}$  depends on the vacuum permittivity  $\epsilon_0$ , the relative permittivity of the medium exposed to the electric field  $\epsilon_{r,M}$ , electrode area  $A$  and the distance between electrodes  $l$ .

$$C_{Geo} = \epsilon_0 \epsilon_{r,M} \frac{A}{l} = \frac{\epsilon_0 \epsilon_{r,M}}{K} \quad (1)$$

As the effective  $A/l$  ratio may be hard to discern for a given electrode geometry it is usually condensed into a generalized geometry factor  $K$ . The interpretation of  $C_{Geo}$  is the primary focus of DEM.

The migration current passing through the electrode setup due to the movement of charge carriers to their respective countercharged electrode surface is accounted for in the lower branch of ECM 1. It is comprised of the solution resistance  $R_s$  in series with the double layer effect  $CPE_{DL}$ .  $R_s$  depends on the electrolytic conductivity of the sample electrolyte  $\kappa_s$  as well as geometrical constraints imparted by the electrode setup which can be expressed with the same geometry factor  $K$  as in equation (1).

$$R_s = \frac{1}{\kappa_s} \cdot \frac{l}{A} = \frac{K}{\kappa_s} \quad (2)$$

As the double layer effect at a solid/electrolyte interface is not purely capacitive in nature, it is usually described with the help of a constant phase element  $CPE_{DL}$ . The frequency domain, in which the impedance response is either dominated by the upper or lower branch of ECM 1 is related to an inverse charge relaxation time constant i.e., characteristic frequency  $f_c$  comprised of  $C_{Geo}$  and  $R_s$ .

$$f_c = \frac{1}{2\pi R_s C_{Geo}} = \frac{1}{2\pi} \cdot \frac{\kappa_s}{\epsilon_0 \epsilon_r} \quad (3)$$

Importantly,  $f_c$  does not depend on the electrode geometry but rather on the intrinsic material property  $\kappa_s/\epsilon_0\epsilon_r$ . An electrolyte which is exposed to ac frequencies  $f_{ac} \gg f_c$  will behave as a dielectric medium with the lower branch in ECM 1 being virtually irrelevant for its impedance response. Conversely, for  $f_{ac} \ll f_c$  the upper branch in ECM 1 will only have a negligible impact on the

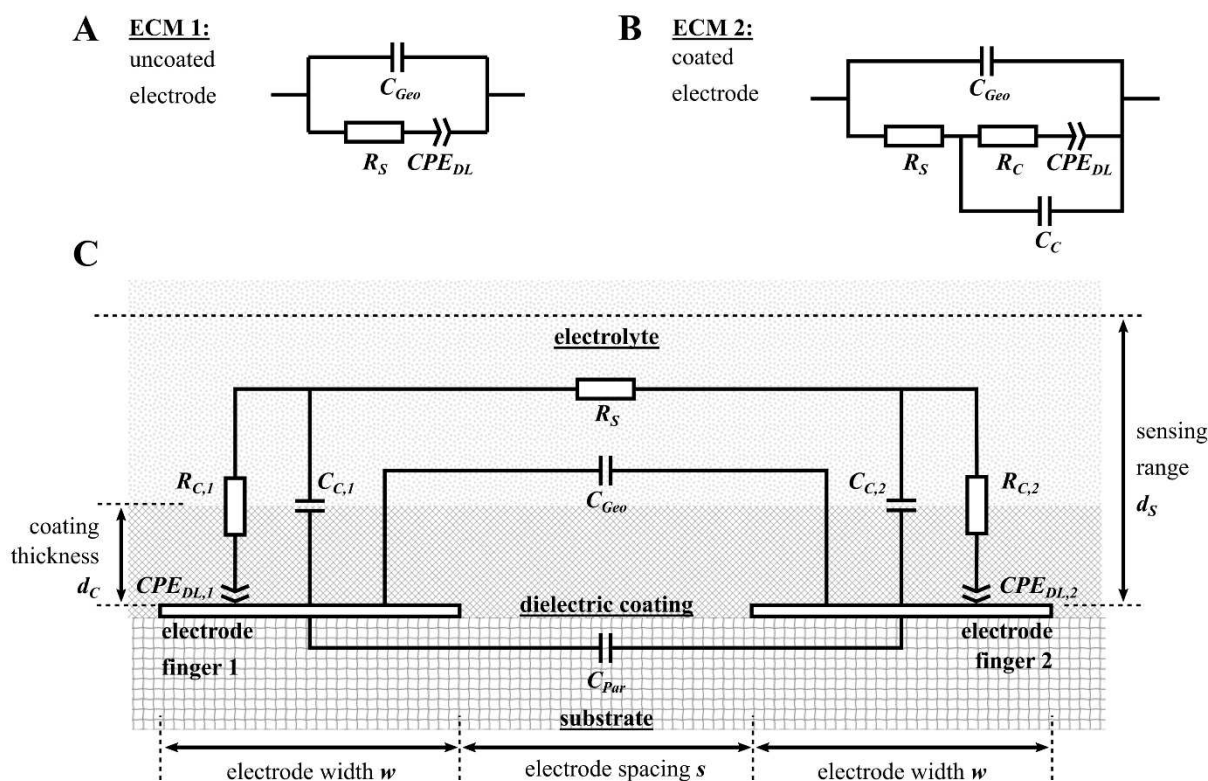


Fig. 1. Basic equivalent circuit models (ECMs) that can be used as a starting point for the interpretation of impedance data taken under non-faradaic conditions for (A) uncoated (ECM 1) and (B) coated electrodes (ECM 2). To facilitate the understanding in the context of interdigitated electrodes (IDEs), a projection of ECM 2 onto the schematic cross section of two electrode fingers is provided in (C).

impedance. A joint interpretation of impedance data by DEM and EIS therefore requires  $f_c$  to be located within the range of recorded frequencies. However, as  $\kappa_s$  and  $\varepsilon_r$  are expected to behave as a complex function of the frequency in the upper MHz or GHz region [26,27], a reasonable integration of DEM into EIS might not be feasible especially for highly conductive electrolytes.

An intuitive expansion to ECM 1 to account for additional impedance effects imparted by a dielectric layer covering the electrode surface is shown in Figure 1(B) [3]. In ECM 2,  $R_S$  is no longer directly wired to  $CPE_{DL}$  but instead to the coating capacitance  $C_C$  and coating resistance  $R_C$  which are in parallel to each other. From a microscopic perspective, the presence of the dielectric coating interferes with the buildup of the double layer as ionic species which wander to their respective countercharged electrode either accumulate at the outer surface of the dielectric layer ( $C_C$ ) or penetrate the film through pores, pinholes, cracks etc. towards the electrode surface ( $R_C$ ). The value of  $C_C$  depends on the coated electrode area  $A_C$ , the coating thickness  $d_c$  and permittivity of the dielectric layer  $\varepsilon_0\varepsilon_{r,C}$ .

$$C_C = \varepsilon_0\varepsilon_{r,C} \frac{A_C}{d_c} \quad (4)$$

In addition to the emergence of  $C_C$  and  $R_C$ , a dielectric coating also affects  $C_{Geo}$  in equation (1). The change in capacitive response can be described in a straightforward way by replacing  $\varepsilon_{r,M}$  in equation (1) to an effective bulk relative permittivity  $\varepsilon_{r,eff}$  whose value ranges between  $\varepsilon_{r,M}$  and  $\varepsilon_{r,C}$ .

$$\varepsilon_{r,eff} = \gamma\varepsilon_{r,C} + (1 - \gamma)\varepsilon_{r,M} \quad (5)$$

The linear interpolation parameter  $\gamma$  shown in equation (5) however represents an intricate function of  $\varepsilon_{r,M}$ ,  $\varepsilon_{r,C}$  as well as the geometrical relationship of both media within the electrode geometry. For this reason, interpretation of  $\varepsilon_{r,eff}$  for dielectric mixtures usually relies on numerical modelling [28,29].

A schematic projection of ECM 2 onto the cross section of two IDE fingers coated with a dielectric layer is shown in Figure 1(C). The electrode geometry of an IDE structure is usually characterized by its metallization ratio  $\eta$  and spatial wavelength  $\lambda$ , both of which depend solely on the electrode finger width  $w$  and spacing  $s$  [30].

$$\eta = \frac{w}{s + w} \quad (6)$$

$$\lambda = 2 \cdot (s + w) \quad (7)$$

The cell constant  $K$  of an IDE geometry is accessible based on the work of Zaretsky et al. [15]. An explicit formula for  $K$  was first published by Olthuis et al. [31]. Similarly, it is possible to derive an expression for the effective permittivity  $\epsilon_{r,eff}$  in equation (5) as a function of  $d_C$ ,  $\epsilon_{r,M}$  and  $\epsilon_{r,C}$  for an IDE geometry with the theoretical model derived by Dias and Igreja [30,32] (see section S4 for more details). The theoretical computation of  $K$  and  $\epsilon_{r,eff}$  assumes an idealized IDE geometry with negligible finger thickness.

An IDE structure is sensitive only to effects occurring in close proximity to its electrode fingers. The sensing range  $d_S$ , also referred to as the effective electric field penetration depth, extends roughly  $\lambda/4$ – $\lambda/3$  into the half planes above and below the electrode fingers [33]. At the first glance, it may appear counterintuitive to assume equality of  $K$  in equations (1) and (2) when working with IDEs since the displacement current penetrates both half planes whereas E-field induced movement of solvated ions is only possible in the upper half plane containing the sample electrolyte. This circumstance however does not pose a problem to the evaluation of the impedance data in case the geometric capacitance of the lower half plane containing the electrode substrate is declared to contribute to the parasitic capacitance  $C_{Par}$  which then needs to be determined prior to the actual experimentation. When comparing ECM 2 in Figure 1(B) with its projection on the IDE cross section shown in Figure 1(C) it is important to highlight that the values of  $C_C$ ,  $R_C$  and  $CPE_{dl}$  in ECM 2 are to be understood as an effective serial expression of the electrochemical phenomena occurring at both counter-charged electrodes. This is because there is no effective difference between counter and working electrode as opposed to conventional EIS setups.

ECM 2 was intentionally conceptualized with the number of circuit elements as small as possible to serve as a starting point for interpretation of impedance data obtained with a dielectrically coated electrode geometry. Depending on the complexity of the system under investigation, it may become reasonable to add extra circuit elements provided they have a clear physical meaning. One commonly encountered extension is the modelling of the coating capacitance as a constant phase element similar to the double layer effect. While this treatment increases the quality of fit between an ECM for any given experimental data, the conversion of the CPE model parameters into an effective capacitance value, which is required to gain access to  $d_C$  and  $\epsilon_{r,C}$ , is controversial [34,35] and would require knowledge on the physical origin of the non-ideally capacitive behavior [36–39]. An effect which has been neglected in ECM 2 is the ionic movement along E-field lines running exclusively through the dielectric film. The neglect is reasonable for  $d_C \ll d_S$ , as the ionic mobility i.e., electrolytic conductivity inside the thin film is expected to be much smaller than in the liquid phase above.

## 3 Experimental Section

### 3.1 HKUST-1 SURMOF Synthesis and Growth Monitoring

The synthesis of the metal organic framework HKUST-1 coating is based on two precursor solutions denoted as “metal” and “linker” solution and a rinsing solution. We used 1 mM copper (II) acetate (Alfa Aesar, USA) in ethanol (VWR, USA) as metal and 0.2 mM benzene tricarboxylic acid (Alfa Aesar) dissolved in 75 % ethanol, 25 % water (mol-%) as linker solution. A 75 % ethanol, 25 % water mixture also served as the rinsing solution. The presence of water in the linker and rinsing solution was previously reported to be of pivotal importance for the successful synthesis of HKUST-1 SURMOFs [40,41]. Prior to the coating experiment, the IDE sensor was cleaned by cyclic voltammetry from  $-1.0$  to  $1.3$  V at a sweep rate of  $0.1$  V/s in  $0.05$  M sulfuric acid (VWR) followed by a 72-hour immersion in a 10/90 volumetric mixture of acetic acid (Sigma Aldrich, USA) and ethanol containing  $20$   $\mu$ M mercaptohexadecanoic acid (Sigma Aldrich) for thiol functionalization of the gold surface. SURMOF coating of the IDEs was carried out in a cycle-by-cycle method in which the electrodes were sequentially exposed to the metal and linker solution, with a rinsing step in between [19]. Every growth cycle was comprised of a 600 s metal – 15 s rinsing – 900 s linker – 15 s rinsing sequence resulting into a highly self-limited growth. The targeted flow rate amounted to  $1$   $\mu$ L/s during metal and linker step and  $10$   $\mu$ L/s during the rinsing step. Impedance spectra were taken during the final 30 s of both the metal and linker step during the first and afterwards every fifth cycle by applying an ac amplitude of  $10$  mV rms. The Gamry Echem Analyst software (Version 7.8.2) allowed fitting of the impedance data to an equivalent circuit model. The error propagation throughout the data analysis was accounted for with a Monte-Carlo method, a detailed description can be found in section S5. All values are reported with their respective  $2\sigma$  error margin.

### 3.2 Setup

The experimental setup is shown in Figure 2. A pneumatic pressure system OB1 MK3 (Elveflow, France) was used to pump the synthesis solutions through a flow selection valve (Rheodyne MHP 7970-500-4 mounted into Qmix V Valve, Cetoni, Germany) into a custom-built polymeric flow cell housing a commercially available ED-IDE3-Au IDE chip (Micrux Technologies, Spain). The spatial wavelength  $\lambda$  of the IDE geometry amounted to  $20$   $\mu$ m with the metallization ratio  $\eta$  estimated at  $0.54$ . The electrode pads of the IDE chip were contacted to a reference 600+ potentiostat (Gamry Instruments, USA) with the help of pogo pins (two electrode setup). To mitigate the effect of external noise, the flow cell was placed inside a Faraday cage. A python script allowed full automation of the system.

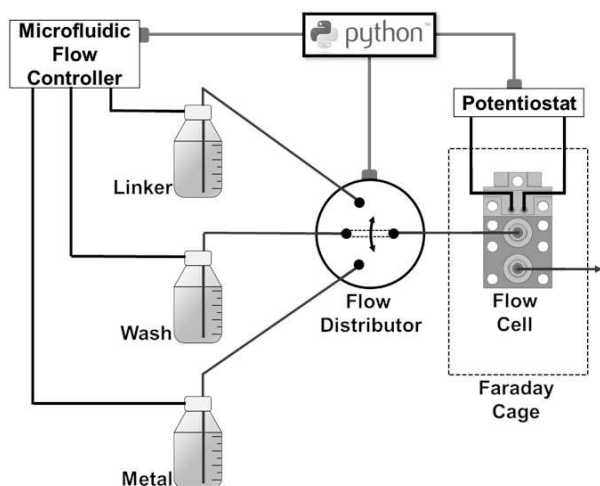


Fig. 2. Schematic showing the setup for the on-line impedimetric monitoring of an HKUST-1 SURMOF growing on IDEs.

### 3.3 Scanning Electron Microscopy (SEM)

SEM micrographs were obtained with a Philips XL30 ESEM (Philips, Netherlands) operating at 20 kV acceleration voltage. Prior to imaging, samples were sputter-coated with a 5 nm conductive platinum layer using a BAL-TEC MED 020 (BAL-TEC AG, Liechtenstein). Cross sections of the IDE geometry were prepared with hammer and chisel.

## 4 Results and Discussion

Interpretation of the impedance data as outlined in section 2 requires knowledge of the cell constant  $K$ , which is directly linked to the solution resistance  $R_S$  and geometric capacitance  $C_{Geo}$ . From a geometrical perspec-

tive,  $K$  is inherently tied to the metallization ratio  $\eta$  and the spatial wavelength  $\lambda$  together with the number and length of electrode fingers and as such can be calculated accordingly. Olthuis et al. however reported a typical discrepancy between the expected and observed  $K$  of 10–20% which was attributed to fringing effects [31]. Another factor which mitigates the applicability of a theoretical model for  $K$  lies in the deviation from the ideal IDE geometry which can be seen in the SEM image of the tilted cross section of a pristine IDE in Figure 3(A). The edges of the electrode fingers are not ideally rectangular, which is likely to be a side effect of the lift-off process during manufacturing as postulated by Timmer et al. [42]. For this reason, we decided to determine  $K$  experimentally with 1-butanol ( $\epsilon_r = 18.19 \pm 0.04$ ) [27], ethanol ( $\epsilon_r = 25.16 \pm 0.04$ ) [27] and air ( $\epsilon_r = 1.00 \pm 0.00$ ) at 20 °C as calibration standard media. The calibration is based on three individual measurements of the impedance response per reference medium at a total of ten frequency points between 1–2 MHz. Under these conditions, the impedance signal is capacitive and can be modelled as  $C_{Geo}$  in parallel to  $C_{Par}$ .

$$Z_{imag} = -\frac{1}{2\pi f_{ac}(C_{Geo} + C_{Par})} = -\frac{1}{2\pi f_{ac}\left(\frac{\epsilon_0 \epsilon_r M}{K} + C_{Par}\right)} \quad (8)$$

Least square fitting of the calibration data to eq (8) results into  $K = (1.68 \pm 0.01) \text{ m}^{-1}$  and  $C_{Par} = (24.1 \pm 0.3) \text{ pF}$ .

The gold surface of the electrode fingers was functionalized with a mercaptohexadecanoic acid self-assembled monolayer (SAM) to facilitate HKUST-1 growth on the gold surface of the electrode. A SAM layer is reported to directly contribute to the double layer capacitance [43] and as such does not need to be accounted for with an additional equivalent circuit element in ECM 1 or 2. Due

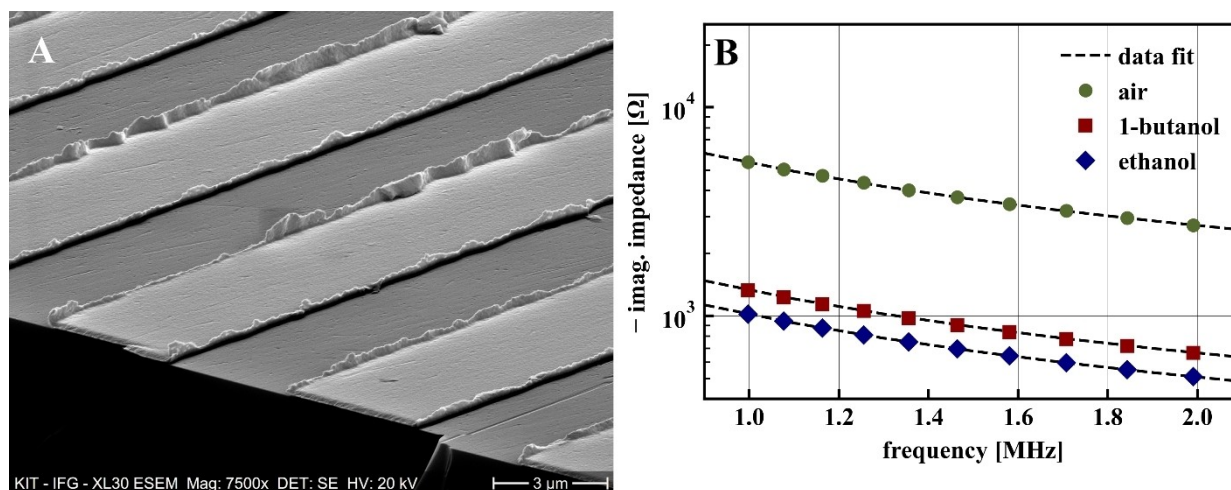


Fig. 3. (A) SEM micrograph of the tilted cross section of an uncoated IDE. The roughened edges which deviate from the ideal IDE geometry are likely caused during the lift-off step of the production process. The cell constant  $K$  was determined experimentally by using air, anhydrous 1-butanol and ethanol as dielectric calibration standards as shown in (B). The calibration data was fitted to equation (8) to obtain  $K$  as well as the parasitic capacitance  $C_{Par}$  imposed primarily by the electrode substrate.

to its limited spatial extension of a few nanometer, the influence of the dielectric SAM layer on  $C_{Geo}$  is assumed to be negligible. The relative permittivity values as well as the electrolytic conductivities of the pristine metal and linker precursor solutions are shown in Table 1. The precursor solutions exhibit characteristic relaxation frequencies which make them eligible to serve as sample media under which both branches of ECM 1 are clearly visible within frequency range typically employed in EIS measurements ( $<5$  MHz).

The impact of a thin dielectric film covering the electrodes on the current response as observed by impedance spectroscopy is given in Figure 4 showing the data taken after the first, 40, 100 and 200 growth cycles during the final seconds of the exposure step to the linker and metal precursor solutions respectively. We observe a

decrease in current response i.e., a rise in impedance across all frequencies during both metal and linker data with an increasing amount of growth cycles completed. The most prominent effect in Figure 4 is visible at frequencies below  $f_c$ , where the dielectric film acts as a diffusion barrier for ions approaching the electrodes. When taking a look at the phase angle data during the first linker and metal step in (B) and (D) we observe a phase angle peak which results from the transition from capacitive ( $C_{Geo}$ ) to resistive ( $R_S$ ) to capacitive ( $CPE_{DL}$ ) behavior from high to low frequencies. Interestingly, the presence of the dielectric thin film after 50, 100 and 200 growth cycles appears to have a quite different impact on the development of the phase angle data recorded during linker and metal step. The initial phase angle peak visible in the linker phase angle data in Figure 4(B) seems to be split in two: a less pronounced peak at around 5 kHz which shrinks in size and a second peak below 1 kHz which moves towards smaller frequencies as the number of growth cycles increases. In contrast, the phase angle peak recorded during the metal cycle in Figure 4(D) decreases in size with no second peak visible. With regard to the expected impedance behavior conceptualized in ECM 2, we infer that the phase angle peak which shrinks as the growth cycles progress is to be identified with the

Table 1. Relative Permittivity, electrolytic conductivity and characteristic frequency of the precursor solutions.

|                 | $\epsilon_r$ [-] | $\kappa_S$ [nS/cm] | $f_c$ [kHz]    |
|-----------------|------------------|--------------------|----------------|
| linker solution | $30.4 \pm 0.1$   | $476 \pm 10$       | $28.2 \pm 0.6$ |
| metal solution  | $25.3 \pm 0.1$   | $620 \pm 8$        | $44.1 \pm 0.5$ |

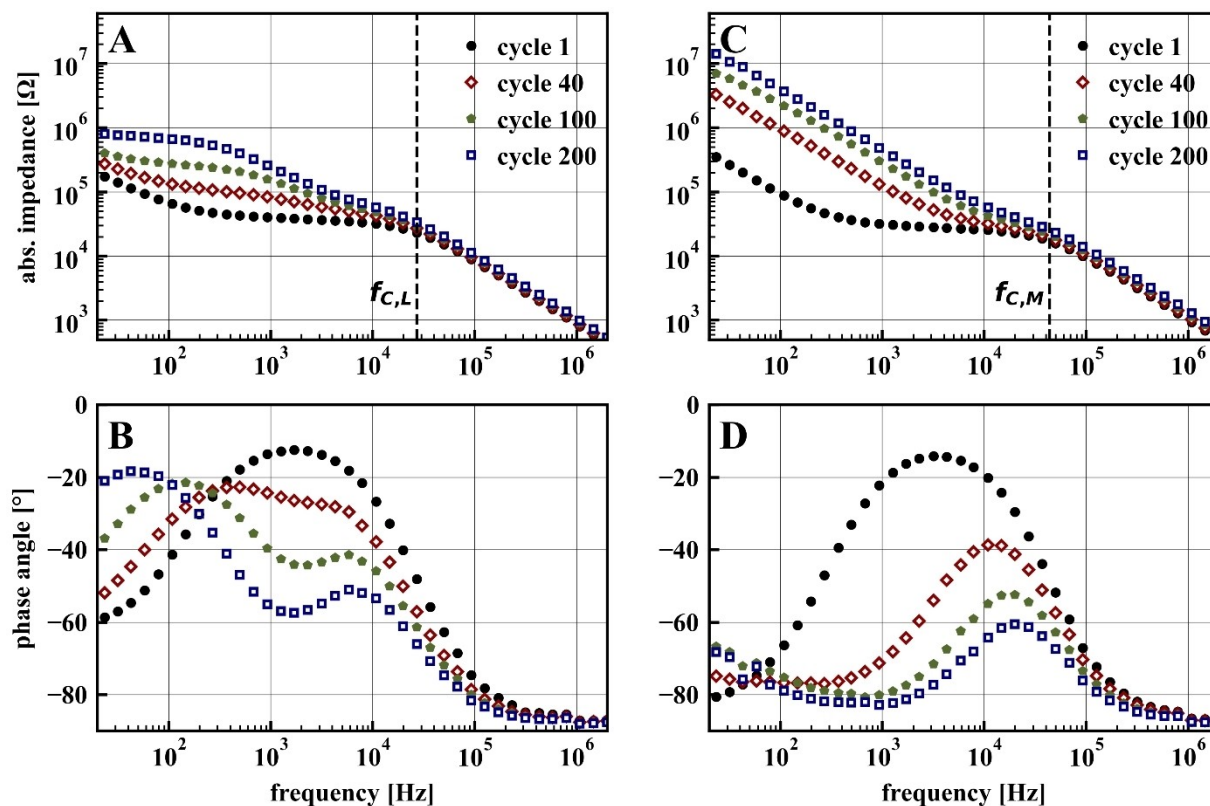


Fig. 4. Impedance data taken during the linker (A)+(B) and metal (C)+(D) step at the end of growth cycles 1, 40, 100, 200. The absolute impedance is plotted in the top row whereas the phase angle is shown in the bottom row. The characteristic frequencies  $f_c$  of the pristine metal and linker precursor solution are inserted to mark the transition from dielectric to electrolytic behavior in the impedance spectrum. The change in impedance response clearly indicates the formation of a dielectric thin film on the electrode surface.

charging of the coating capacitance  $C_C$  visible in both metal and linker impedance spectra. We thus assign the occurrence of the second phase angle peak at smaller frequencies to the charging of the double layer effect. The absence of the second phase peak during the metal cycle data indicates a reduced ionic permeability of the dielectric layer. This is supported by the fact that the absolute impedance recorded at frequencies below 1 kHz increases by roughly two orders of magnitude during the metal steps in comparison to a rise by the factor of four during the linker steps over the course of 200 growth cycles. The moderate increase in the phase angle visible at frequencies below 1 kHz during the metal step after 100 and 200 growth cycles which is not present after 40 cycles is unlikely to be identified with any effect accounted for in ECM 2. For this reason, we chose to limit the ECM 2 fit to the impedance data recorded during the metal step to the frequency range between 2–2000 kHz to obtain the coating capacitance  $C_{C,MS}$  and solution resistance  $R_{S,MS}$  while setting the coating resistance  $R_{C,MS}$  to infinity. By contrast, as the underlying electrochemical phenomena of the impedance data taken during the linker step appeared to be sufficiently represented in ECM 2, we imposed no frequency range and parameter restriction to the ECM fit to the linker data.

$C_{C,MS}$  as well as  $C_{C,LS}$  are plotted in Figure 5(A). We chose not to include the initial 35 growth cycles as for the resulting material deposited on the electrode, the determination of  $C_C$  involves great uncertainties which might be related to the underlying Volmer-Weber growth mechanism reported in earlier studies [44,45]. SURMOF synthesis is initiated by heterogeneous nucleation of individual crystallite islands at the surface which grow in size leading to an eventual coalescence into a pinhole free layer under the formation of grain boundaries. After coalescence, the HKUST-1 SURMOF is reported to grow in a self-limiting “layer-by-layer” fashion [46–48]. Both

$C_{C,M}$  and  $C_{C,L}$  decrease hyperbolically as a function of completed growth cycles which in accordance with equation (4) would suggest a linear increase in layer thickness. Interestingly,  $C_{C,LS}$  is not equal to  $C_{C,MS}$  but rather consistently 2.0–2.4 times larger than its counterpart during the metal step. Especially during the final 100 cycles the ratio appears to have converged to a constant value of  $2.3 \pm 0.1$ . With regard to equation (4), both a significant change in relative permittivity of the dielectric layer e.g., due to absorption of water into the internal pores or a substantial difference in layer thickness e.g., due to adsorption of precursor molecules at the outer surface and/or reversible swelling (breathing) of the SURMOF layer could explain the observed difference in  $C_C$ . To elucidate whether there is a sizeable difference in layer thickness during linker and metal cycle it is reasonable to take a look at  $R_S$  which is plotted in Figure 5(B).  $R_S$  is inversely proportional to the sum of ionic movement inside the liquid phase exposed to the electric field as outlined in equation (2). The increase in  $R_S$  in Figure 5(B) can be primarily attributed to an increased volume fraction occupied by the dielectric layer, i.e., reduction in space for free ionic movement in the liquid phase within the IDE sensing range  $d_S$ . Most importantly, the increase in solution resistance during the linker step  $R_{S,L}$  is similar to  $R_{S,MS}$  observed during the metal step. While initially amounting to  $1.30 \pm 0.03$ , their ratio  $R_{S,LS}/R_{S,MS}$  does not change substantially throughout the SURMOF growth standing at  $1.41 \pm 0.06$  after 205 cycles. For this reason, it is safe to assume there is no significant difference in layer thickness between metal and linker step meaning the cause of the difference in  $C_C$  is primarily found in the difference in coating permittivity during metal  $\epsilon_{r,C,MS}$  and linker  $\epsilon_{r,C,LS}$  steps and thus  $C_{C,LS}/C_{C,MS} = 2.3 \pm 0.1 = \epsilon_{r,C,LS}/\epsilon_{r,C,MS}$ . The initial increase of  $C_{C,LS}/C_{C,MS}$  during cycles 40–100 is likely to be identified with the differential increase in layer thickness

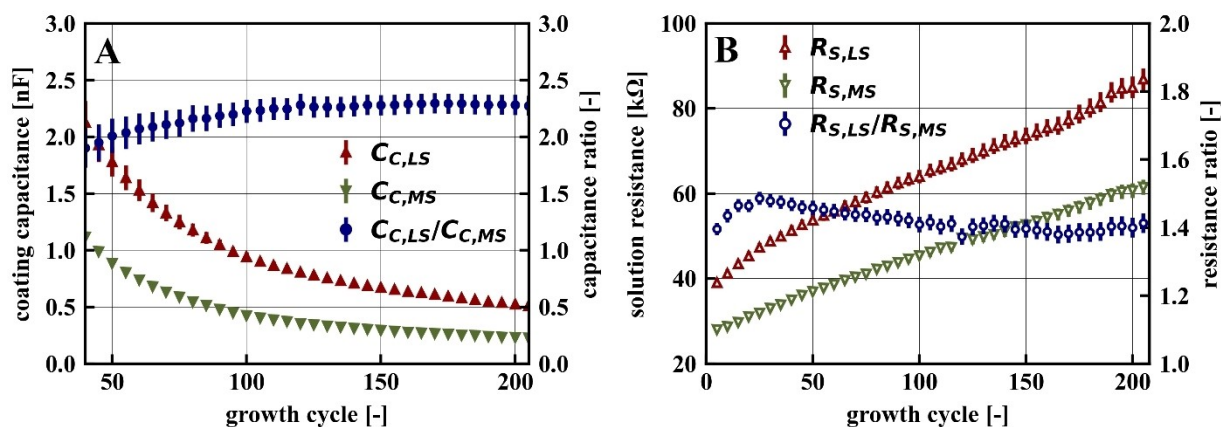


Fig. 5. (A) Coating capacitance  $C_C$  and (B) solution resistance  $R_S$  as a function of the growth cycle during the linker and metal step as well as their respective ratio. Both the decrease of  $C_C$  and the increase  $R_S$  as more and more growth cycles are being completed hint towards steady growth of the dielectric HKUST-1 thin film which as a result occupies an ever-increasing volume fraction within the IDE sensing range. The near constant ratio of  $C_{C,LS}/C_{C,MS}$  of  $2.3 \pm 0.1$  during the final 100 growth cycles indicates a reversible change in the dielectric properties of the thin film when exposed to the metal and linker precursor solution.

occurring between metal and linker step within the same growth cycle. The smaller the differential increase in layer thickness between metal and linker step during the same growth cycle compares to the layer thickness already grown, the smaller its impact on  $C_{C,LS}/C_{C,MS}$  and  $R_{S,LS}/R_{S,MS}$  which would explain their convergence roughly from cycle 100 onwards. The minor peak of the  $R_{S,LS}/R_{S,MS}$  ratio observed after 25 growth cycles in Figure 5(B) could be related to modelling difficulties of the ECM fit during the early island growth stage of the SURMOF synthesis.

In addition to the more obvious effects of thin film growth on the frequency domain below  $f_c$ , the presence of the thin film in the electrode sensing space also induces a change in  $C_{Geo}$  visible in the upwards movement of the impedance data at frequencies above  $f_c$  in Figure 4(A) and (B) as the growth cycles progress. The shifting of the impedance curve to higher values implies a decrease in  $C_{Geo}$  i.e.,  $\epsilon_{r,eff}$  in equation (5) as the dielectric layer occupies an increasingly large volume fraction within the electrode sensing range. Similar to the calibration method,  $C_{Geo}$  can be obtained directly from the purely capacitive impedance response between 1–2 MHz which is virtually unaffected from effects related to the lower branch of ECM 2. In this way  $C_{Geo}$  is determined with greater accuracy than an ECM fit to the entire frequency spectrum would provide as the fit is subject to numerical errors as well as minor measurement inaccuracies imposed for example through the adjustment of the current measurement range during the recording of the spectrum. The effective relative permittivity in the IDE sensing range during the linker  $\epsilon_{r,eff,LS}$  and metal step  $\epsilon_{r,eff,MS}$  as calculated with equation (8) from  $C_{Geo}$  is plotted in Figure 6(A). Over the course of 205 growth cycles,  $\epsilon_{r,eff,LS}$  drops from initially  $30.4 \pm 0.1$  to  $23.5 \pm 0.1$  by 22.7% whereas  $\epsilon_{r,eff,MS}$  drops from initially  $25.3 \pm 0.1$  to  $17.1 \pm 0.1$  by 32.4%. Interpretation of  $\epsilon_{r,eff,LS}$  and  $\epsilon_{r,eff,MS}$  in accord-

ance to equation (5) to gain direct access to  $\epsilon_{R,C,LS}$  and  $\epsilon_{R,C,MS}$  requires a method to obtain the linear interpolation parameter during the linker  $\gamma_L(cycle)$  and metal  $\gamma_M(cycle)$  steps. While theoretical models for  $\epsilon_{r,eff}$  of a coated IDE geometry exist, they are based on the same geometric assumptions as the theoretical computation of  $K$ . Due to the non-ideality of the IDE geometry we opted for a heuristic approach by assuming  $\gamma_{MS}(cycle) \approx \gamma_{LS}(cycle)$  which can be combined with the ratio  $\epsilon_{r,C,LS}/\epsilon_{r,C,MS} = 2.3 \pm 0.1$  as obtained from the ECM data fit to calculate  $\epsilon_{r,C,MS}$  and  $\epsilon_{r,C,LS}$  with the help of equation (5). When averaging the data of the final 100 growth cycles, we arrive at  $\epsilon_{r,C,MS} = 6.8 \pm 0.5$  and  $\epsilon_{r,C,LS} = 15.3 \pm 0.5$ . The relative permittivity of an activated HKUST-1 single crystal was recently reported by Babal et al. as 2.8 [23]. Ethanol saturation of the porous single crystal resulted into an increase of the relative permittivity to 7.5 during the first and 7.4 during the second inclusion cycle [23]. Correspondingly, the value for  $\epsilon_{r,C,MS}$  could therefore be explained by the presence of solvent molecules (ethanol) in the crystalline voids of the porous, dielectric layer. The slightly smaller value of  $\epsilon_{r,C,MS}$  in comparison to the values reported by Babal et al. might be related to a difference in structural defect densities between the polycrystalline thin film and the single crystal. On the other hand, the disparity between  $\epsilon_{r,C,MS}$  and  $\epsilon_{r,C,LS}$  could be linked to the solvent composition of the purely ethanolic metal solution and the linker solution containing 25 mol-% water. With the relative permittivity of a water saturated HKUST-1 single crystal reported at approximately 64 [23], the value of  $\epsilon_{r,C,LS}$  would suggest the presence of both ethanol and water molecules in the porous structure. The reproducible change in  $\epsilon_{r,C}$  when exposed to the precursor solutions throughout the synthesis process is a strong hint towards reversible access of guest (solvent) molecules into the internal pores of the HKUST-1 layer.

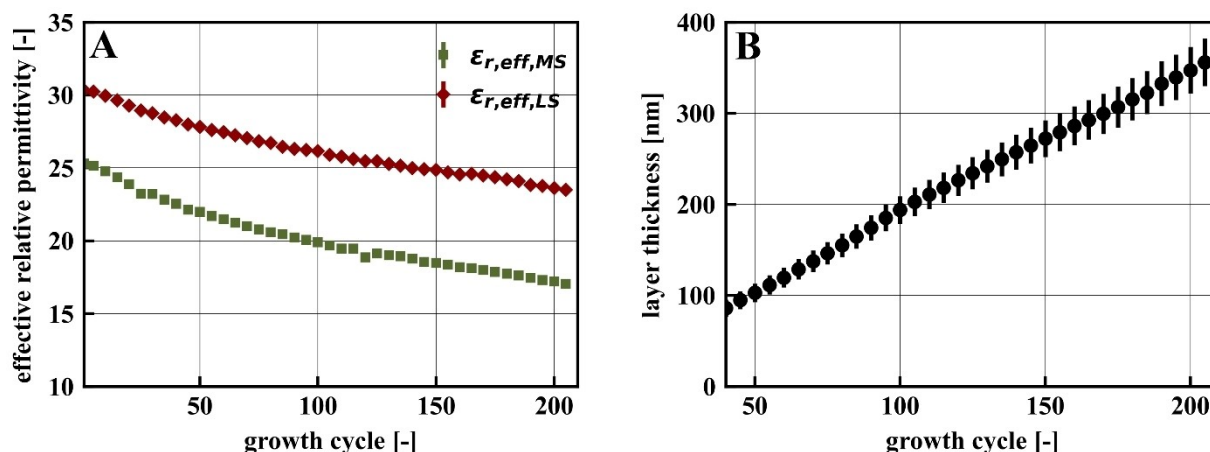


Fig. 6. (A) Effective relative permittivity  $\epsilon_{r,eff}$  within the IDE sensing range as a function of the completed growth cycles during both the metal and linker precursor solution. The joint interpretation of  $\epsilon_{r,eff}$  and  $C_{C,LS}/C_{C,MS} = 2.3 \pm 0.1$  with the help of equation (5) allows access to the dielectric properties of the thin film and in turn its layer thickness which is plotted in (B). The impedimetric characterization of the HKUST-1 SURMOF growth indicates a near linear growth rate of  $(1.5 \pm 0.2)$  nm/cycle.

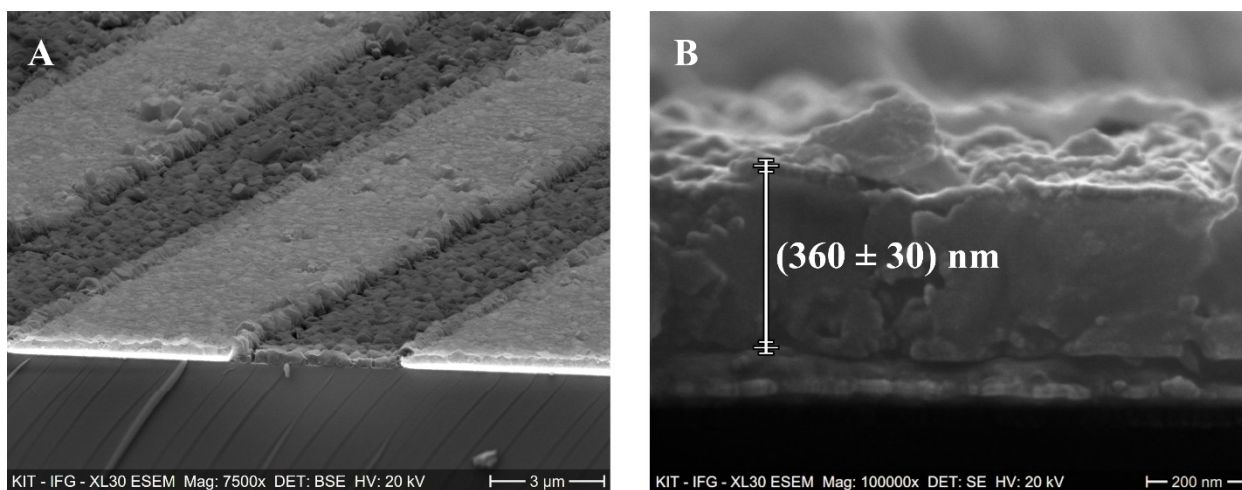


Fig. 7. SEM micrographs of the coated IDE geometry after 205 growth cycles. The backscattered electron (BSE) signal was used to image the tilted cross section shown in (A). As the BSE contrast mode allows discrimination between regions of different atomic mass, the completely coated gold electrode fingers can easily be identified. A closeup of the coating cross section is shown in (B) which was taken with the secondary electron detector. For comparative reasons, the final layer thickness after 205 cycles  $d_C = (360 \pm 30)$  nm as estimated by the evaluation of the impedimetric growth data is projected onto the micrograph which corresponds well to the observed layer thickness.

The combination of  $\varepsilon_{r,C}$  and  $C_C$  with the total horizontal electrode surface area  $A_e$  estimated in chapter S2 as  $(5.4 \pm 0.3)$  mm<sup>2</sup> provides access to the coating thickness  $d_C$ .

$$d_C = \varepsilon_0 \varepsilon_{r,C} \frac{A_e}{4C_C} \quad (9)$$

The factor 4 located in the denominator of equation (9) derives from the effective serial connection of the coating capacitances acting at both the counter and working electrodes as illustrated in Figure 1(C) and Figure S3. Due to the strongly self-limiting cycle by cycle growth mechanism of the HKUST-1 SURMOF,  $d_C$  increases linearly as a function of the completed growth cycles as illustrated in Figure 6(B). The averaged growth rate from cycle 40–205 amounts to  $(1.5 \pm 0.2)$  nm/cycle.

To examine the accuracy of the layer thickness estimate provided by our impedimetric evaluation method, we imaged the coated IDE geometry by SEM. The micrograph shown in Figure 7(A) was obtained with the backscattered electron (BSE) signal. The BSE contrast mode allows mapping of the sample into regions of different atomic weight providing a clear distinction between the golden electrode fingers and the copper-organic based HKUST-1 SURMOF coating. The electrode surfaces in Figure 7(A) are fully covered by the HKUST-1 SURMOF with no cracks or pinholes present. This observation agrees well with the divergent behavior observed between the low frequency impedance data recorded during the metal and linker step visible in Figure 4. A high magnification secondary electron micrograph of the HKUST-1 SURMOF cross section is provided in Figure 7(B). The estimated thickness is

projected onto the micrograph which agrees well with spatial extension of the SURMOF layer.

Before we conclude our findings, let us briefly recapitulate the surplus value obtained through the combination of DEM and EIS with regard to the example showcased above. If we had focused exclusively on the frequency range below  $f_c$  and applied data fit to the lower branch of ECM 2 we would have arrived at the ratio  $\varepsilon_{r,C,LS}/\varepsilon_{r,C,MS}$  with no direct access to either  $\varepsilon_{r,C,LS}$ ,  $\varepsilon_{r,C,MS}$  and as such  $d_C$  as well. Likewise, a purely dielectric evaluation of the growth data at frequencies well above  $f_c$  by DEM would have led into a similar dead end with no constitutive connection between  $\varepsilon_{r,C,LS}$  and  $\varepsilon_{r,C,MS}$ . Even worse, the usual assumption of the same dielectric properties of the thin film when exposed to two separate dielectric reference media i.e.,  $\varepsilon_{r,C,LS} = \varepsilon_{r,C,MS}$  would have caused a severe misinterpretation of the growth process.

## 5 Conclusion

We demonstrated that integration of dielectrometry into electrochemical impedance spectroscopy allows for a thorough characterization of dielectric thin films. The essential prerequisite for the joint interpretation is to have access to impedance data covering a frequency range above and below the characteristic relaxation frequency, which depends on the ratio of electrolytic conductivity divided by the permittivity. In addition, both the reference medium and the dielectric thin film should comprise a non-negligible volume fraction within the electrode setup. The impedimetric evaluation routine outlined in this work allowed us to successfully monitor the growth of an HKUST-1 SURMOF on an interdigitated electrode geometry. The results clearly reveal a linear increase in

the film thickness as a function of the completed growth cycles. The conversion of impedance data into film thickness could be validated by scanning electron microscopy. Furthermore, the reversible change in the relative permittivity value of the HKUST-1 SURMOF thin film when exposed to the linker and metal precursor solutions hint towards a significant uptake of guest molecules into the nanoporous coating. For this reason, we are confident that the joint analysis of electrochemical impedance spectroscopy together with dielectrometry will provide innovative opportunities for the characterization of novel materials as well as future sensing applications using porous dielectrics.

## CRedit Authorship Contribution Statement

**Benedikt Sapotta:** Conceptualization, Methodology, Formal Analysis, Data Curation, Visualization, Software, Investigation, Resources, Writing – Original Draft. **Matthias Schwotzer:** Visualization, Resources. **Matthias Franzreb, Christof Wöll:** Supervision, Project administration Funding acquisition. All authors contributed to the writing – review & editing process.

## Supporting Information

Details of the flow cell used, the determination of the electrode surface area, analytical model for the calculation of the effective relative permittivity of a coated IDE, application of coating capacitance to IDE structures, error propagation method, coating resistance during the linker step and XRD-Data of the coated IDE.

## Abbreviations

|         |  |
|---------|--|
| ac      | alternating current  |
| BSE     | backscattered electrons  |
| DEM     | dielectrometry   |
| ECM     | equivalent circuit model   |
| EIS     | electrochemical impedance spectroscopy                                       |
| HKUST-1 | Hongkong University of Science and Technology – 1, a metal organic framework |
| IDE     | interdigitated electrode   |
| SAM     | self-assembled monolayer   |
| SEM     | scanning electron microscopy   |
| SURMOF  | surface mounted metal organic framework                                      |

## Symbols

|            |  |
|------------|--|
| $A$        | electrode area                             |
| $A_e$      | total electrode surface area               |
| $C_C$      | coating capacitance                        |
| $C_{C,LS}$ | coating capacitance during the linker step |
| $C_{C,MS}$ | coating capacitance during the metal step  |
| $C_{Geo}$  | geometric capacitance                      |
| $C_{Par}$  | parasitic capacitance                      |

|                       |   |
|-----------------------|---|
| $CPE_{DL}$            | constant phase element to model the double layer effect     |
| $d_C$                 | coating thickness   |
| $d_S$                 | sensing range of the IDE geometry                           |
| $\epsilon_r$          | relative permittivity                                       |
| $\epsilon_{r,C}$      | relative permittivity of the coating                        |
| $\epsilon_{r,C,LS}$   | relative permittivity of the coating during the linker step |
| $\epsilon_{r,C,MS}$   | relative permittivity of the coating during the metal step  |
| $\epsilon_{r,eff}$    | effective relative permittivity                             |
| $\epsilon_{r,eff,MS}$ | effective relative permittivity during the metal step       |
| $\epsilon_{r,eff,LS}$ | effective relative permittivity during the linker step      |
| $\epsilon_{r,M}$      | relative permittivity of a reference medium                 |
| $\epsilon_0$          | vacuum permittivity (8.854e–12 F/m)                         |
| $\eta$                | metallization ratio of the IDE geometry                     |
| $f_{AC}$              | frequency of the alternating current                        |
| $f_C$                 | characteristic relaxation frequency                         |
| $\gamma$              | linear interpolation parameter in equation (5)              |
| $K$                   | geometry factor of the electrode geometry                   |
| $\kappa_s$            | electrolytic conductivity                                   |
| $l$                   | distance between electrodes                                 |
| $\lambda$             | spatial wavelength of the IDE geometry                      |
| $R_C$                 | coating resistance  |
| $R_S$                 | solution resistance   |
| $R_{S,LS}$            | solution resistance during the linker step                  |
| $R_{S,MS}$            | solution resistance during the metal step                   |
| $s$                   | electrode spacing of the IDE geometry                       |
| $w$                   | electrode width of the IDE geometry                         |

## Acknowledgements

This work was supported by the Deutsche Forschungsgemeinschaft (DFG, German Research Foundation) under Germany's Excellence Strategy – 2082/1 – 390761711. Open access funding enabled and organized by Projekt DEAL.

## Data Availability Statement

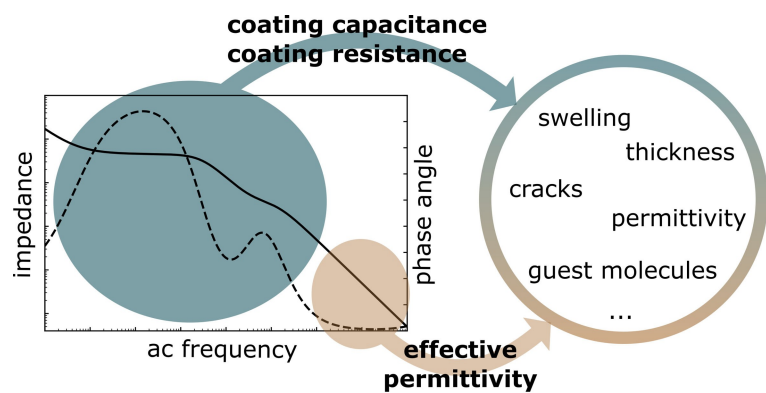
The data that support the findings of this study are openly available on Mendeley Data at <https://doi.org/10.17632/d6g8zyj8r5.2>.

## References

- [1] J. J. Suay, E. Giménez, T. Rodriguez, K. Habib, J. J. Saura, *Corros. Sci.* **2002**, *45*, 611–624.
- [2] P. L. Bonora, F. Deflorian, L. Fedrizzi, *Electrochim. Acta* **1996**, *41*, 1073–1083.
- [3] F. Mansfeld, *J. Appl. Electrochem.* **1995**, *25*, 187–202.
- [4] K. Jüttner, *Electrochim. Acta* **1990**, *35*, 1501–1508.
- [5] J. M. McIntyre, H. Q. Pham, *Prog. Org. Coat.* **1996**, *27*, 201–207.
- [6] F. Mansfeld, *Electrochim. Acta* **1990**, *35*, 1533–1544.

- [7] R. Igreja, C. J. Dias, *Mater. Sci. Forum* **2006**, 514–516, 1064–1067.
- [8] T. Islam, A. T. Nimal, U. Mittal, M. U. Sharma, *Sens. Actuators B* **2015**, 221, 357–364.
- [9] J. Boudaden, A. Klumpp, I. Eisele, C. Kutter, *IEEE Sensors*, Orlando, FL, USA **2016**.
- [10] R. Igreja, C. J. Dias, *Sens. Actuators B* **2006**, 115, 69–78.
- [11] X. Fang, O. K. Tan, M. S. Tse, E. E. Ooi, *Biosens. Bioelectron.* **2010**, 25, 1137–1142.
- [12] L. Yang, Y. Li, G. Erf, *Anal. Chem.* **2004**, 76.
- [13] J. M. Pingarrón, J. Labuda, J. Barek, C. M. A. Brett, M. F. Camões, M. Fojta, D. B. Hibbert, *Pure Appl. Chem.* **2020**, 92, 641–694.
- [14] M. C. Zaretsky, P. Li, J. R. Melcher, *IEEE Trans. Electr. Insul.* **1989**, 24, 1159–1166.
- [15] M. C. Zaretsky, L. Mouard, J. R. Melcher, *IEEE Trans. Electr. Insul.* **1988**, 23, 897–917.
- [16] A. Dizon, M. E. Orazem, *Electrochim. Acta* **2019**, 327.
- [17] A. Dizon, M. E. Orazem, *Electrochim. Acta* **2020**, 337.
- [18] J. Hong, D. S. Yoon, S. K. Kim, T. S. Kim, S. Kim, E. Y. Pak, K. No, *Lab Chip* **2005**, 5, 270–279.
- [19] O. Shekhah, H. Wang, S. Kowarik, F. Schreiber, M. Paulus, M. Tolan, C. Sternemann, F. Evers, D. Zacher, R. A. Fischer, C. Wöll, *J. Am. Chem. Soc.* **2007**, 129, 15118–15119.
- [20] J. Getzschmann, I. Senkovska, D. Wallacher, M. Tovar, D. Fairen-Jimenez, T. Düren, J. M. van Baten, R. Krishna, S. Kaskel, *Microporous Mesoporous Mater.* **2010**, 136, 50–58.
- [21] S. Okur, P. Qin, A. Chandresh, C. Li, Z. Zhang, U. Lemmer, L. Heinke, *Angew. Chem. Int. Ed. Engl.* **2021**, 60, 3566–3571.
- [22] K. N. Chappanda, O. Shekhah, O. Yassine, S. Patole, M. Eddaoudi, K. N. Salama, *Sens. Actuators B* **2018**, 257.
- [23] A. S. Babal, A. K. Chaudhari, H. H. M. Yeung, J. C. Tan, *Adv. Mater. Interfaces* **2020**, 7.
- [24] A. M. Ullman, C. G. Jones, F. P. Doty, V. Stavila, A. A. Talin, M. D. Allendorf, *ACS Appl. Mater. Interfaces* **2018**, 10, 24201–24208.
- [25] L. Kreno, J. Hupp, R. Duyne, *Anal. Chem.* **2010**, 82.
- [26] T. Yamaguchi, T. Matsuoka, S. Koda, *J. Chem. Phys.* **2007**, 127, 234501.
- [27] A. P. Gregory, R. N. Clark, *NPL Report MAT 23* **2012**, .
- [28] K. K. Kärkkäinen, A. Sihvola, K. Nikoskinen, *IEEE TGRS* **2000**, 38, 1303–1308.
- [29] C. J. Dias, R. Igreja, *Sens. Actuators A Phys.* **2017**, 256, 95–106.
- [30] R. Igreja, C. J. Dias, *Sens. Actuators A Phys.* **2004**, 112, 291–301.
- [31] W. Olthuis, W. Streekstra, P. Bergveld, *Sens. Actuators B* **1995**, 24–25, 252–256.
- [32] R. Igreja, C. J. Dias, *Sens. Actuators A Phys.* **2011**, 172, 392–399.
- [33] C.-u. Kim, G. Li, J. Li, H. Jong, C. Ro, Y. Song, G. Pak, S. Im, *J. Phys. Conf. Ser.* **2013**, 418.
- [34] P. Zoltowski, *J. Electroanal. Chem.* **1998**, 443, 149–154.
- [35] M. E. Orazem, I. Frateur, B. Tribollet, V. Vivier, S. Marcelin, N. Pébère, A. L. Bunge, E. A. White, D. P. Riemer, M. Musiani, *J. Electrochem. Soc.* **2013**, 160, C215–C225.
- [36] B. Hirschorn, M. E. Orazem, B. Tribollet, V. Vivier, I. Frateur, M. Musiani, *Electrochim. Acta* **2010**, 55, 6218–6227.
- [37] C. L. Alexander, B. Tribollet, V. Vivier, M. E. Orazem, *Electrochim. Acta* **2017**, 251, 99–108.
- [38] C. L. Alexander, B. Tribollet, M. E. Orazem, *Electrochim. Acta* **2016**, 188, 566–573.
- [39] C. L. Alexander, B. Tribollet, M. E. Orazem, *Electrochim. Acta* **2015**, 173, 416–424.
- [40] K. Muller, J. Singh Malhi, J. Wohlgemuth, R. A. Fischer, C. Woll, H. Gliemann, L. Heinke, *Dalton Trans.* **2018**, 47, 16474–16479.
- [41] Z. Wang, K. Rodewald, R. Medishetty, B. Rieger, R. A. Fischer, *Cryst. Growth Des.* **2018**, 18, 7451–7459.
- [42] B. Timmer, W. Sparreboom, W. Olthuis, P. Bergveld, A. van den Berg, *Lab Chip* **2002**, 2, 121–124.
- [43] F. R. Castiello, J. Porter, P. Modarres, M. Tabrizian, *Phys. Chem. Chem. Phys.* **2019**, 21, 15787–15797.
- [44] M. L. Ohnsorg, C. K. Beaudoin, M. E. Anderson, *Langmuir* **2015**, 31, 6114–6121.
- [45] A. Summerfield, I. Cebula, M. Schroder, P. H. Beton, *J. Phys. Chem. C* **2015**, 119, 23544–23551.
- [46] C. Munuera, O. Shekhah, H. Wang, C. Woll, C. Ocal, *Phys. Chem. Chem. Phys.* **2008**, 10, 7257–7261.
- [47] O. Shekhah, *Materials* **2010**, 3, 1302–1315.
- [48] Q. Zhang, Y. Pramudya, W. Wenzel, C. Woll, *Nanomaterials (Basel)* **2021**, 11.

Received: August 23, 2021  
Accepted: November 8, 2021  
Published online on ■■, ■■



*B. Sapotta, M. Schwotzer, C. Wöll,  
M. Franzreb\**

1 – 12

**On the Integration of Dielectrometry into Electrochemical Impedance Spectroscopy to Obtain Characteristic Properties of a Dielectric Thin Film**

